

Error Sources and Feasibility for Microwave Remote Sensing of Ocean Surface Salinity

**Simon H. Yueh, Richard West, William J. Wilson, Fuk K. Li, Eni G. Njoku, and
Y. Rahmat Samii**

**Jet Propulsion Laboratory
California Institute of Technology
4800 Oak Grove Drive
Pasadena, CA 91109
Tel: (818) 354-3012, Fax: (818) 393-5285**

Abstract

A set of geophysical error sources for the microwave remote sensing of ocean surface salinity have been examined. The error sources include the sea surface temperature, sea surface roughness, atmospheric gases, ionospheric Faraday rotation, and solar and galactic emission sources. It is shown that the brightness temperature errors of a few Kelvin can be expected for most of these error sources. The key correction requirements for accurate salinity measurements are the knowledge accuracy of 0.5°C for the sea surface temperature (SST), 10°C for the surface air temperature, 0.2° accuracy for the Faraday rotation, and surface roughness equivalent to $0.3\text{ m}\cdot\text{s}^{-1}$ for the surface wind speed. We suggest the use of data products from AMSR-type instruments for the corrections of SST and liquid cloud water, the numerical weather analysis for the air temperature, coincidental radar observations with 0.2 dB precision for surface roughness and on-board polarimetric radiometer channel for Faraday rotation. The most significant sky radiation is from the sun. A careful design of the antenna is necessary to minimize the leakage of solar radiation or reflection into the antenna sidelobe. The narrow-band radiation from galactic hydrogen clouds with a bandwidth of less than 1 Mhz is also significant, but can be corrected with an accurate radio sky survey or minimized with a notched (band-rejection) filter centered at 1.420 GHz in the receiver. The other planetary and galactic radio sources can be flagged with negligible data loss. We have performed a sampling analysis for a polar-orbiting satellite with 900 km swath width to determine the number of satellite observations over a given surface grid cell during an extended period. Under the assumption that the observations from different satellite passes are independent, it is suggested that an accuracy of 0.1 psu is achievable for global monthly 1-degree latitude and 1-degree longitude gridded products.

1 Introduction

Global measurements of sea surface salinity (SSS) are important for studying the ocean circulations and rainfall and consequently for improving the estimates of seasonal to interannual climate predictions. Three broad primary scientific objectives for SSS remote sensing have been proposed by the Salinity Sea Ice Working Group (SSIWG) [1]: 1) Improving seasonal to interannual climate predictions, where assimilating SSS combined with other parameters has been shown to have a positive impact on coupled forecasts, 2) improving ocean rainfall estimates and global hydrologic budgets, where the oceanic mixed layer freshwater budget is reflected in SSS variability and can be used to balance surface freshwater flux, and 3) monitoring large scale salinity events, in particular, tracking interannual SSS variability in the Nordic Seas, which influences oceanic thermohaline convection and heat transport, and is vital to long term climate prediction and modeling. The measurement of global ocean surface salinity is viewed as a missing element in the ocean modeling and flux studies.

The specific accuracy requirements for these cases vary with the space and time scales of the phenomena to be resolved. An Earth explorer mission for ocean surface salinity has been recommended in the National Aeronautics and Space Administration (NASA) post-2002 mission plan with an accuracy of 0.2-0.3 psu at better than 100 km resolution for weekly global mapping. In addition, the European Space Agency has selected the Soil Moisture/Ocean Salinity (SMOS) Mission as an Earth explorer mission for launch in 2005-2006 [13].

The principle of satellite SSS remote sensing has been thoroughly described in [2]. It is based on the sensitivity of sea surface brightness temperatures (T_b) to SSS at microwave frequencies. The sea surface T_b is a product of the sea surface emissivity and the sea surface temperature (SST). The surface emissivity is a function of the water dielectric constant, which is by itself a function of the salinity, temperature, and radio frequencies. It has been pointed out by [2] that lower radio frequencies have a better sensitivity to the salinity, but are more sensitive to the ionospheric Faraday rotation and require a larger antenna aperture

to maintain the same spatial resolution. A reasonable compromise is the choice of the 1.4 GHz (L-band) frequency band set aside for radio astronomy use.

The challenge for the SSS remote sensing is that the L-band sea surface T_b is influenced by many geophysical parameters, such as sea surface roughness, sea surface temperature, ionospheric Faraday rotation, solar radiation, and atmospheric gases (Fig. 1). The effects of most of these parameters are comparable to the sensitivity of T_b to SSS.

The concept of microwave SSS remote sensing has been demonstrated by many airborne microwave systems [3, 4, 5, 6]. It was demonstrated that the effects of sea surface temperature could be eliminated by using two frequency channels at L- and S-bands [3]. A transect flight with the airborne Electronically Scanning Thin Array Radiometer (ESTAR) noted an SSS change of a few psu from seaward of the Gulf Stream to Cape Hatteras [4]. Aircraft flights to map the coastal salinity [5, 6] indicated a reasonable agreement between the microwave measurements and the SSS observations from the ship thermosalinograph, but there could be differences as large as 1-3 psu. An error of a few psu is acceptable for coastal oceans, where the dynamic range of salinity is significant, but is too large for open ocean conditions with salinity in the range of 32 to 37 psu. It remains a challenge to establish the remote sensing technique for global SSS measurements.

To meet the accuracy requirements of SSS remote sensing from space, a thorough understanding of various error sources is required. The analysis by [2] provided a general discussion on the effects of ocean surface roughness, atmospheric oxygen, solar radiation, galactic background, and ionosphere. Since that analysis, additional experimental work has been carried out to improve the sea water dielectric model [9] and to more accurately determine the influence of atmosphere [17] and surface roughness. Also the effects of various parameters, in particular the ionosphere and emissions from our solar system and galaxy, depend on the satellite viewing geometry and antenna characteristics, and necessitates a more quantitative evaluation for specific instrument configurations. This paper will present an extensive analysis of these parameters and will identify algorithms to estimate and correct

the effects of these error sources (Section 2). To estimate the accuracy of weekly or monthly averaged satellite SSS products, the number of satellite passes over a given surface grid cell is estimated with an orbit propagator and a simulation of antenna scanning geometry (Section 3). We also examine the sampling requirements for a space instrument necessary to meet the desired SSS accuracy requirements.

2 Measurement principle and Error Sources

The sources of microwave radiation are illustrated in Fig. 1. This section examines the effects of these parameters at L-band frequencies.

2.1 Measurement Sensitivity

In the past, the sensitivity of microwave radiation to water salinity was studied primarily using the dielectric constant model proposed by Klein and Swift [8], denoted as the KS model hereafter. The passive microwave observations from the SSM/I have suggested a reasonable accuracy of the KS model, but there could be a bias of up to a few Kelvins above 19-GHz frequencies [10]. This is not surprising because the KS model was derived from measurements acquired at frequencies lower than X-band (10 GHz). The latest effort to improve the dielectric constant model of sea water was undertaken by [9] with new laboratory measurements covering a large range of frequencies, temperature, and salinity. This new model, denoted as the Ellison model, has been shown to provide a better agreement with satellite microwave observations of sea surfaces [10].

The Ellison model has been used to examine the vertically and horizontally polarized brightness temperatures (T_v and T_h) of a smooth water surface at 1.4 GHz. Fig. 2 illustrates the dependence of T_v and T_h of a smooth surface on the surface salinity at 40° incidence angle and six water temperatures. Note that the brightness temperatures are more sensitive to SSS for warmer and more saline waters. The two lower panels plot the derivatives of T_v and T_h as a function of SSS. For the surface salinity of open oceans (typically greater than

30 psu), the sensitivity is in the range of 0.35 to 0.8 Kelvin/psu for vertical polarization and 0.2 to 0.6 Kelvin/psu for horizontal polarization. The vertical polarization is about 30% more sensitive to the SSS than the horizontal polarization.

Fig. 3 illustrates the dependence of brightness temperatures on the surface salinity as a function of incidence angle for a water salinity of 35 psu at six water temperatures. The vertical polarization becomes more sensitive to the water salinity at higher incidence angles, while the horizontal polarization exhibits an opposite trend. The characteristics are similar for cold and warm waters. Interestingly, the average of the vertically and horizontally polarized brightness temperatures, illustrated in the bottom panel, is almost insensitive to the incidence angle. This suggests that a broad range of incidence angles is potentially useful for the remote sensing of ocean surface salinity. Other factors, such as the influence of sea surface roughness and antenna footprint resolution, have to be considered to select the incidence angles for a satellite mission. We have performed similar calculations with the KS model. The results are very similar to the predictions from the Ellison model.

2.2 Sea Surface Temperature

The derivative of T_b with respect to water temperature is illustrated versus incidence angle for six water temperatures (T_s) and a salinity of 35 psu (Fig. 4). There is a small polarization dependence with the vertical polarization (upper panel) being more sensitive to the water temperature than the horizontal polarization for cold waters ($< 10^\circ\text{C}$) and high incidence angles ($> 40^\circ$). The average of T_v and T_h derivatives illustrated in the bottom panel is almost insensitive to the incidence angle.

For cold waters ($T_s < 10^\circ\text{C}$), the derivative of T_b with respect to T_s is positive, indicating that T_b increases with increasing water temperature, while a negative derivative for warm waters ($T_s > 20^\circ\text{C}$) indicates a decreasing trend. At the nominal water temperature of 15°C , T_b is almost insensitive to the change of water temperature. These characteristics are about the same from 0° to 60° incidence angles. In general when the water temperature varies by

1°C, T_b can vary by about ± 0.1 K for SSS in the range of 32 to 37 psu. (Fresher water has a stronger temperature dependence of up to 0.5 K per degree C change, not illustrated here.)

2.3 Atmosphere dry air and water vapor

To investigate the effects of the atmosphere for realistic conditions, we used the Liebe's millimeter wave propagation model (MPM) [17] to estimate the microwave emission and attenuation from numerical weather products. The numerical weather products were the reanalyses produced by the National Center for Environmental Prediction (NCEP). The reanalyses consist of the vertical profiles of air temperature, humidity, geopotential height, and winds at 17 pressure levels on 2.5° latitude by 2.5° longitude global grid. The temperature and humidity profiles at each grid point were the input to the MPM model for the estimates of the atmospheric transmissivity (β), upwelling radiation (T_u) on the top of atmospheric layer and downwelling radiation at the surface (T_d) at 1.4 GHz and 40° incidence angle.

We find that T_u and T_d are almost identical with a difference of less than 0.002 Kelvin. This is due to the small loss of atmosphere at low microwave frequencies; therefore the weighting factor due to the atmospheric absorption loss versus altitude has a negligible influence on the integration of radio emissions along the path. We also find that the water vapor has a very small contribution at 1.4 GHz. The dominant contribution is from the dry air, resulting in an upwelling and downwelling radiation of about 2.4 to 2.8 Kelvins. T_u , T_d and β have a small correlation with the surface air temperature at 1000 mb (T_a). Fig. 5 provides a scatter plot of the estimates from twelve daily NCEP grids on the 15th of every month in 1995. We have excluded the data over land surfaces from the analyses. An examination of the MPM model suggests that the loss of dry air continuum due to nonresonant O_2 spectrum below 10 GHz decreases with increasing temperature, consistent with what is plotted in Fig. 5. A detailed evaluation of the MPM model suggests the data scatter is due to the variations of temperature and pressure profiles. Fig. 5 also provides the mean and standard deviation of the scatter for every 5° C bin. The standard deviation

is about 0.015 Kelvin for warm surfaces ($T_a \geq 25^\circ \text{ C}$) and is about 0.1 Kelvin for cold surfaces ($T_a \leq 10^\circ \text{ C}$). This suggests that if the surface air temperature is known, then the atmospheric radiation can be predicted with an accuracy of better than 0.1 Kelvin.

We use the MPM model outputs and the columnar water vapor height (V) and T_a to generate an empirical model for the upwelling and downwelling radiation, and the propagation loss

$$\alpha = a_0 + a_1 T_a + a_2 T_a^2 + bV \quad (1)$$

where V is in cm and T_a is in $^\circ\text{C}$. A least square error criterion is used to find the coefficients of the empirical model (Table 1). It is shown that the water vapor has a negligible contribution at the L-band frequencies with an influence of less than 0.01 K for the maximum columnar water vapor height, which is about 6 cm. The T_a dependence, dominated by the quadratic term, has a small linear dependence.

If we use this empirical model together with the numerical weather analyses to correct satellite observations, the residual error will be limited by how well we know the surface temperature T_a and the modeling uncertainty indicated by the error bar in Fig. 5. For a surface temperature of below 10° C , the mean values of brightness temperatures are relatively insensitive to the surface temperature, implying that an accurate knowledge of the surface temperature is not required. To further minimize the modeling uncertainty, the vertical profiles of air temperature and pressure in the weather analyses have to be considered for the data corrections.

2.4 Cloud

At L-band frequencies, the cloud radiation and scattering can be well accounted for by the Rayleigh scattering model [17]. We used the propagation model for clouds described in the MPM model to estimate the path-integrated propagation loss and radiation. Fig. 6 illustrates the cloud radiation and attenuation versus the integrated liquid water content for -10° to 10° C along the vertical path. It is shown that the clouds are more lossy and radiative at

lower temperatures. The cloud radiation is less than 0.06 K at L-band for an integrated liquid water path (LWP) of less than 0.3 mm, which generally represents the upper limit of the LWP product derived from the Special Sensor Microwave/Imager.

If we simply assume a data correction with average cloud radiation, the residual error would be less than 0.03 K at 0° incidence angle and 0.04 K at 40° incidence angle, except for precipitating conditions. A more accurate approach is to use the cloud liquid water products from AMSR- or SSM/I-type systems, operating in close temporal proximity. In consideration of the dynamical variations of cloud covers, the issue is whether coincidental observations are required. For climate modeling studies, which only require weekly or monthly averaged SSS products, this is not expected to be an issue because the weekly or monthly average of AMSR-type satellite products would allow an accurate removal of cloud emissions.

2.5 Surface Roughness

Experimental evidence on the effects of surface roughness on L- and S-band microwave brightness temperatures of sea surfaces can be found in [7, 14, 15, 16]. A comparison of these data sets acquired in 1970s and 1980s was well summarized in [18]. Table 2 summarizes some of the results from these earlier studies together with recent aircraft radiometer measurements [22]. These observations suggest that the L-band sea surface brightness temperatures increase by a few tenths of Kelvins for an increase of wind speed by 1 m/s. The horizontal polarization is clearly more sensitive to the wind speed than the vertical polarization at above 40° incidence angles. Thus, an uncertainty of 1 m·s⁻¹ wind speed will lead to an error of about a few tenths to 1 psu, depending on the incidence angle, polarization, water temperature and salinity (Figs. 2 and 3). It is apparent that the surface roughness induced by winds have to be corrected to enable an accurate SSS retrieval, especially for cold waters.

With these observations, there are still issues about the dependence of brightness temperatures on surface roughness. Numerous observations and theoretical analyses have indicated that the roughness of sea surfaces is affected not only by winds, but also by many other

factors, such as swell, surface temperature, and fetch [19, 20]. As noted in Table 2, Swift's measurements [14] indicate a significantly stronger wind speed sensitivity than the observations by Hollinger [7]. The discrepancy could be the result of different sea states: Hollinger's experiment was conducted on Argus Island tower, located approximately 45 km off Bermuda, while Swift's set up was in the Cape Cod Canal.

To examine the influence of surface roughness effects on ocean surface salinity retrieval, JPL has developed a Passive/Active L-/S-band (PALS) dual-polarized microwave radiometer and radar. This system was deployed on the National Center for Atmospheric Research (NCAR) C-130 aircraft for three flights on July 17-19, 1999, across the Gulf Stream off Norfolk, Virginia. The in-situ measurements were performed by the Duke University's research vehicle Cape Hatteras. The ship data indicated that the wind speed near and across the Gulf Stream was low and highly variable in the range of 0-6 m·s⁻¹ on July 17. It appeared that the aircraft flight track had intercepted several areas with smooth surfaces across and near the Gulf Stream front. Fig. 7 illustrates one set of coincidental radiometer and radar measurements made at a 40° incidence angle. The area with a smooth surface is indicated by a low radar backscatter (about -30 dB for vertical polarization and -45 dB for horizontal polarization.) The radiometer results also decrease over the same area. T_v and T_h change by about 1.4 and 2.4 Kelvins, respectively, across the region with a sharp surface roughness (perhaps wind) gradient. Under the assumption of a linear relationship and a change of wind speed by 6 m·s⁻¹, the slope of brightness temperature versus wind speed is 0.23 K/m·s⁻¹ for vertical polarization and 0.40 K/m·s⁻¹ for horizontal polarization. For this case study, the JPL data provide support to Swift's horizontally polarized data (Table 2), while JPL's results are more sensitive to the surface roughness than Hollinger's for both polarizations. If we assume that the data from all three sources are correct, the conflicts among them suggest the influence of other mechanisms, in addition to the winds, on the roughness of sea surfaces.

The JPL data set suggests that the direct information of surface roughness can be provided by microwave radar backscatter. By comparison with radiometer observations, the

radar backscatter of sea surfaces is sensitive to surface roughness, but nearly insensitive to SST and SSS, and provides independent information of surface roughness to enable the correction of radiometer observations. We have examined the brightness temperature versus the normalized radar cross sections (σ_0) for vertically polarized transmit and receive (σ_{vv}) and horizontally polarized transmit and receive (σ_{hh}). A quasi-linear relationship appears between the excess brightness temperatures (ΔT_b) and σ_0 . Under the approximation of Bragg scattering for sea surfaces, ΔT_b and σ_0 are both proportional to the spectrum of sea surfaces; therefore it is reasonable to adopt a linear relationship, $\Delta T_b = A\sigma_0$. The feasibility of using radar data to correct the brightness temperatures is suggested by this linear model. The upper panel in Fig. 7 plots the uncorrected and corrected brightness temperatures using σ_{hh} with $A = 240$ for T_v and 400 for T_h . The moderate change of brightness temperatures is reduced (Fig. 7). The two lower panels in Fig. 7 illustrate the SSS retrieved from the brightness temperature data plotted in the upper panel. The SSS estimates from T_v without correction have a change of about 1 psu across the front and the estimates from T_h without correction change by about 3 psu. These changes correlate with the variations of surface roughness. The estimates from the corrected brightness temperature data, illustrated in the bottom panel, do not have such a salinity gradient. (The ship data acquired from multiple transects at different latitudes across the Gulf Stream front to the west of the flight line are plotted as a reference.) Because the salinity was not expected to have a significant change to the east of the Gulf Stream front, the results support the feasibility of using radar data for surface roughness correction. Based on the coincidental radar and radiometer data illustrated in Fig. 7, a precision of 0.2 dB for σ_{vv} and σ_{hh} measurements will provide a better than 0.1 Kelvin accuracy for ΔT_b correction.

The previous data sets [7, 18] and the JPL aircraft PALS measurements also indicate the possibility of utilizing the polarization diversity to reduce the effects of surface roughness. This algorithm explores the differing polarization behavior of brightness temperatures, which indicates that a linear combination of T_v and T_h at above 40° incidence can eliminate the

effects of surface roughness. For example, the quantify, $T_{b1} = T_v - aT_h$, would be less dependent on wind speed, with $a = 0.6$ appearing to be a good choice at 40° incidence. The coefficient “ a ” is expected to be closer to one for smaller incidence angles and decreases with increasing incidence angles. The major drawback is that T_{b1} is about a factor of two less sensitive to SSS than T_v (Table 3). The derivative of T_{b1} with respect to SSS reduces to about 0.45 K/psu at 30°C water temperature and about 0.2 K/psu at 5°C water temperature.

2.6 Ionosphere

The effects of Faraday rotation has been examined by many investigators, for example [23]. It has been suggested that the Faraday rotation could cause several Kelvins of errors for linearly polarized measurements. To enable an accurate correction of the Faraday rotation an effective technique based on the polarimetric radiometry has been proposed in [23]. Here, the results from [23] is summarized for completeness.

As the microwave radiation from the earth surface propagates through the ionosphere, the linearly polarized field components are rotated by an angle Ω (Faraday rotation), depending on the geomagnetic field and ionospheric electron content. Under the influence of Faraday rotation, the polarization of the microwave radiation is rotated, and the detected brightness temperature by the antenna will be different from the surface radiation by ΔT_B .

$$\Delta T_B = (T_v - T_h) \sin^2 \Omega - \frac{U}{2} \sin 2\Omega \quad (2)$$

where T_v and T_h are the vertically and horizontally polarized brightness temperatures of the surface radiation, and U is the third Stokes parameter of the surface radiation [23]. From the above equation, it is straightforward to show that ΔT_B is less than 0.1 K for a Faraday rotation of less than a few degrees, but can reach above 10 K for a Faraday rotation of 30° at 40° incidence and L-band frequencies.

A technique based on microwave passive polarimetry is described in [23] for the estimates of ionospheric Faraday rotation under the assumption of azimuth symmetry for the surfaces under investigation. This technique includes a third Stokes parameter channel in the space-

borne L-band radiometer together with the traditional vertical and horizontal polarization channels. The third Stokes parameter is a measure of the correlation between vertically and horizontally polarized radiation. Without the Faraday rotation, the correlation between these two polarizations is negligible for sea surfaces at L-band frequencies. As the radio emissions from sea surfaces propagating through the ionosphere, the Faraday rotation creates a polarization mixing or a correlation between these two polarization channels. From the third Stokes parameter measurements, the polarization correlation enables an estimate of the ionospheric Faraday rotation for the corrections of T_v and T_h observations. An error analysis [23] shows that the Faraday rotation can be estimated with an accuracy of better than one degree with a space-based L-band system, and the residual correction errors of linearly polarized brightness temperatures can be less than 0.1 Kelvin. Specifically, the residual error of the brightness temperatures after correction is

$$\Delta T_h \approx \frac{\Delta U \sin 2\Omega}{2} \quad (3)$$

for horizontal polarization. Here ΔU corresponds to the measurement error by the radiometer and the small Stokes parameter of the ocean surface radiation. By assuming a ΔU of 0.2 K, ΔT_h is less than 0.04 K for $\Omega = 10^\circ$, 0.06 K for $\Omega = 20^\circ$ and 0.09 K for $\Omega = 30^\circ$.

From the GPS network observations [24], the ionospheric TEC at 6 am and 6 pm local times is usually less than 30 TECU at above 60° latitudes, and may reach 60 TECU in the equatorial areas. The resulting Faraday rotation at 1.4 GHz will be less than 20° most of the time, and hence the brightness temperature correction errors will be less than 0.06 K.

2.7 Solar System And Galactic Radiation

In this section, the effects of the radio radiation sources within our solar system and galaxy are examined. These include Sun, Moon, planets, galactic background and hydrogen clouds.

2.7.1 Sun

The Sun is an extremely strong radiation source at L-band. The angular extent of the solar disk is about 0.224 deg^2 as viewed from the Earth. Its blackbody temperature (T_{sun}) at L-band could be higher than 10 million K during the peak of the solar cycle, and could be as low as 100,000 K during the quiet period [12]. The next quiet period is expected to be between 2006 and 2008.

There are two mechanisms contributing to the solar radiation intercepted by a microwave receiver: One is the direct leakage into the antenna, and the other is the reflection by the earth surface (Fig. 8). By denoting the apparent antenna temperature of the direct leakage into the antenna by T_{Ad} and that of the surface reflection by T_{Ar} , the total apparent antenna temperature is the sum of these two terms.

For the direct leakage, which enters through the sidelobes of the antenna,

$$T_{Ad} = T_{sun} \frac{\Omega_i}{4\pi} G \quad (4)$$

where Ω_i is the angular extent of the solar disk, and G is the antenna gain at the direction toward the sun. This formula [12], valid for a point source, implicitly assumes that the angular width of the sun is much smaller than the antenna beamwidth.

For the surface reflection, the apparent antenna temperature of the power received by the antenna can be written as:

$$T_{Ar} = T_{sun} \frac{\Omega_i}{(4\pi)^2} \sum_{\alpha} \int \frac{\cos \theta_i}{\cos \theta_s} G \gamma_{\beta\alpha}(\theta_s, \phi_s, \theta_i, \phi_i) d\Omega_s \quad (5)$$

where $\gamma_{\beta\alpha}$ is the bistatic scattering coefficient of the surfaces with α and β indicating the polarization of incident and scattered waves, respectively. θ_i and θ_s are the incidence and scattering angles at the surface, and ϕ_i and ϕ_s are the azimuth angles of incident and scattering directions. $d\Omega_s$ is the differential solid angle of the surfaces viewed from the antenna.

For most natural surfaces, the analytic expression of $\gamma_{\beta\alpha}$ is not available. There are only a few types of rough surfaces, which are simple enough to allow an analytic examination.

The expressions of $\gamma_{\beta\alpha}$ for several types of rough surface scattering mechanisms, including the Bragg scattering and geometric optics, are available in the literature, for example [21]. One type of surface has a large undulation, but a small slope. The scattering from this type of surfaces can be approximated by geometric optics and physical optics. The other type has a small surface roughness and also a gentle slope. The scattering from this type of surfaces can be approximated by Bragg scattering. For ocean surfaces, which have multiple length scales, a combination of the Geometric Optics and Bragg scattering (2-scale scattering) is frequently used to approximate the total surface scattering.

For the case of a smooth surface with a Fresnel reflection coefficient R , γ can be expressed as

$$\gamma = \frac{4\pi|R|^2}{\sin \theta_i} \delta(\theta_s - \theta_i) \delta(\phi_s - \phi_i) \quad (6)$$

The apparent antenna temperature T_{Ar} reduces to:

$$T_{Ar} = T_{sun} \frac{\Omega_i}{4\pi} |R|^2 G \quad (7)$$

for a smooth surface.

The other special case corresponds to a very rough reflective surface with $\gamma = 1$ (isotropic scattering). For this type of surface,

$$T_{Ar} = \gamma T_{sun} \frac{\Omega_i}{4\pi} \frac{1}{2\pi} \int \frac{\cos \theta_i}{\cos \theta_s} G d\Omega \quad (8)$$

If we assume a narrow antenna beam, the integral can be approximated as

$$\int \frac{\cos \theta_i}{\cos \theta_s} G d\Omega \approx \frac{\cos \theta_i}{\cos \theta_s} \int G d\Omega = \frac{\cos \theta_i}{\cos \theta_s} 4\pi \quad (9)$$

where θ_i and θ_s are evaluated at the location pointed by the antenna boresight.

$$T_{Ar} \approx \gamma T_{sun} \frac{\Omega_i \cos \theta_i}{2\pi \cos \theta_s} \quad (10)$$

This formula is a good approximation for the cases that the surface scattering coefficient γ varies slowly over the antenna main beam.

As discussed above, the effects of solar radiation depends on the antenna gain, geometry of the sun illumination and antenna pointing directions, and the surface scattering properties. In the following, we estimate the upper bound of T_A from Sun for a satellite microwave mission concept for ocean salinity and soil moisture [11]. The mission concept [11] assumes a microwave system with a conical-scanning antenna operating at a sun-synchronous polar orbit with an equatorial crossing time at 6 am or 6 pm. For this orbit, the solar radiation is approximately from the direction perpendicular to the orbital plane of the satellite. The orbit altitude is 600 km, and the antenna boresight points at 36° from the spacecraft nadir axis. The antenna considered is an offset parabola with 6 meter diameter. The antenna gain directivity is 37.5 dB, and the beamwidth is 2.8° . For simplicity, we assume a spherical earth for the geometry calculations. The resulting incidence angle is 40° on the surface.

The antenna receives the maximum solar radiation when the antenna beam points toward the Sun in azimuth (Fig. 8). For this configuration, most of the solar energy reflected by the surface comes from two locations (A and B). Location A is pointed by the antenna boresight, and location B is where the sun energy will be specularly reflected. The incidence angle of the solar radiation is 86° at location A, which is 46° from the boresight. The incidence angle at location B is 76° with the specular reflection at 26° from the antenna boresight. The sun is located at 54° from the antenna boresight.

The reflection reaches a maximum when the surface at location A is very rough and reflective and the surface at location B is like a mirror. For this scenario, the total surface reflection can be approximated by the sum of two terms described by Eqs. (8) and (10). Fig. 9 plots these two terms from the surface reflection and the direct leakage. The maximum diffused scattering term [Eq. (10)] could be as high as 0.1 K for the quiet sun and 10 K during the solar maximum. It needs to be emphasized that this is an overestimate for the ocean surface. For ocean surfaces, most of the solar energy is reflected forward in the specular direction at location A, and the remaining reflection into the main antenna beam can be minimized by a modeling of the reflectivity at location A, which is related to the surface

roughness.

During the quiet period of the solar cycle, the specular reflection term, Eq. (8), can be made less than 0.05 K as long as the antenna gain at 26° off the boresight is kept at less than -10 dB, which is achievable for most antennas. During the peak of the solar activity, the antenna gain has to be kept at -30 dB level or lower to maintain the same level of accuracy. It is noted that the direct leakage term takes the same form as the specular reflection term with $R = 1$. The direct leakage term should be smaller because it enters the antenna from the sidelobe at 54° off the boresight, which is further away from the boresight than the angle of specular reflection term.

The other configuration of interests represents the situation that the antenna points at 180° in azimuth from the sun. For this case, the only contribution from the sun is the direct leakage into the antenna sidelobe at 126° from the boresight. As long as the antenna gain at this angle is kept at -30 dB or lower, the contribution of this term is negligible. However, this term is potentially correctable because it only depends on T_{sun} and G . As long as a monitoring of T_{sun} is made and the antenna pattern is stable, a correction would be possible.

The above analysis suggests that the solar radiation poses a significant challenge for the remote sensing of ocean salinity. Its effects seem to be manageable during the quiet period of solar cycle for a properly designed antenna beam pattern. During the solar maximum, the microwave data acquired at a look direction toward the sun will be contaminated, and only the observations away from the sun are useful. For the mission concept described in [11], which considers a 6am/6pm sun-synchronous orbit, the part of the scan where the antenna is looking at the sun is at the edge of the swath. If the data from the part of the scan within $\pm 30^\circ$ toward the sun are rejected, the reduction of the swath width is about 8%, and is a negligible loss of data.

2.7.2 Moon and Planets

The L-band microwave radiation from the Moon is dominated by the thermal blackbody emission. The lunar temperature at L-band is about 200 K with a small variation dependent

on the lunar phase [12]. Although the moon's microwave emission is much smaller than the sun's, it is possible for the lunar radiation to be specularly reflected into the main beam of the antenna on a polar orbiting satellite. Under the assumption of 37.5 dB for the antenna directivity, an angular extent of 0.215 deg^2 for the moon, a surface reflectivity of $R = 1$, and 200 K for lunar temperature, the apparent antenna temperature of the reflected moon emission will be about 5 K [Eq. (7)].

Suppose we flag the data acquired when the specular reflection is near the peak of antenna gain. For the mission concept suggested by [11], the worst-case geometry occurs when the moon is located on the orbit plane of the satellite. Should we use 0.005 K as the threshold, which corresponds to an antenna gain of 7.5 dB (30 dB down from the gain peak). The resulting angular beam width is about 8° , and the percentage of the data that have to be flagged will be about $(8/360)^2$ or about 0.05%.

The emission from the planets in our solar system can be treated in a similar manner. Because these planets have a much smaller angular extent and have also a blackbody temperature of about no more than a few hundred kelvins [12], the effects of the planets are negligible.

2.7.3 Galactic Radio Emissions

The galactic radio emission sources include discrete sources and a background radiation [12]. The galaxy consists of many billions of stars and there are many with strong radio emissions. The apparent continuous distribution of background radiation may consist of the radiation from unresolved discrete sources, thermal emission from ionized hydrogen and nonthermal emission from relativistic particles moving in the galactic magnetic fields.

The L-band emissions from most discrete sources, except Cassiopeia A, Cygnus A, and Crab Nebula, have negligible flux densities at the Earth surface. The flux densities of these three sources are within a factor of about one to three of the moon's (Chapter 8, [12]). Based on earlier discussions, the percentage of the data loss due to these discrete sources would be very small for the satellite mission concept described in [11].

The background radiation is mostly concentrated around the galactic plane. The strongest radiation sources come from the galactic center with about 16 Kelvin at 1.4 GHz. The background radiation also consists of a 2.7 K blackbody spectrum, which was due to the primordial fireball which created the universe. The effects of these background radiation sources are limited to the specular reflection into the main antenna beam. Because of their relative constant amplitudes, a correction can be made with a radio sky survey at 1.4 GHz. The worst case error is due to the galactic center, but the data loss would be small for this case if a data flag is applied.

In addition to the background radiation with a continuous spectrum, there are also narrow band emissions from interstellar neutral hydrogen at around the spectral line of 1.420 GHz. The neutral hydrogen clouds are organized in bands of spiral arms around the galactic center. The Doppler shift due to the relative motion of the hydrogen clouds and the earth and the internal motion of hydrogen gases is within ± 500 kHz. The amplitude of the line profiles is typically less than 100 Kelvins. If we assume a receiver bandwidth of 20 MHz, the equivalent antenna noise temperature will be less than 5 Kelvins. Because the characteristics of the neutral hydrogen in our galaxy are expected to be stable, the hydrogen line emissions can be corrected with a sky survey.

An alternate approach to reduce the effects of hydrogen line is to implement a notched filter with a bandwidth of 1 to 2 Mhz to remove the narrow band radiation. Because the radio bandwidth protected for science observations is 20 Mhz centered at 1.420 GHz, the notched filter reduces the available bandwidth for SSS measurements by about 5 to 10%. The impact on the radiometer NEDT is not too significant, about 5% for inserting a notched filter with 2 Mhz bandwidth into a radiometer utilizing only the protected band. The real tradeoff between the notched filter design and a correction algorithm with the radio sky survey is the complexity of electronics design and cost.

3 Sampling Analysis and Error Estimates for Satellite Instrumentation

The accuracy of weekly or monthly SSS products from orbiting satellites depends on the number of satellite passes over a given grid cell within the period of time. We have conducted a sampling analysis with a satellite instrument retrieval simulator for the mission concept described in [11]. The simulator includes an orbit propagator to simulate the orbiting satellite positions in time and an antenna geometry routine to simulate the antenna scanning geometry. The orbit considered is a sun-synchronous polar orbit at 600 km altitude. The antenna is a 6-m offset parabolic deployable-mesh antenna, and spins around the satellite nadir axis at a rotation rate of 6 rpm. Two feedhorns illuminate this reflector to produce two footprints at 38° and 40° incidence angles. The swath width is about 900 km. Because various geophysical and calibration error sources could be spatially or temporally correlated, the multiple observations made by these two antenna beams within a satellite pass over a given surface grid cell may not be independent. To be conservative, we therefore consider only the number of satellite passes (N) for a surface grid cell within a given duration of time.

Fig. 10(a) plots the number of satellite passes for 1-degree latitude and 1-degree longitude surface grid cells within one week. There is a global coverage with more observations in the high latitude region than in the equatorial region. The number of satellite passes can vary for the surface grid cells at the same latitude. The diamond-shaped patterns indicate the overlapping geometries of multiple satellite passes. Fig. 10(b) illustrates the number of cells versus the number of satellite passes. The cells indicated with no satellite passes actually correspond to the land surface or sea ice cover. The number of satellite passes at between -60° to -70° latitude is in the range of 10 to 20. The equatorial regions have about half of the number of passes.

In the following we estimate the accuracy of satellite SSS measurements from the effects of various error sources at a nominal incidence angle of 40° . Table 3 summarizes the influence of

various geophysical error sources for three water temperature ranges. For each temperature range, the estimated brightness temperature errors are listed for T_v , T_h , $(T_v + T_h)/2$ and $T_v - 0.6T_h$. The estimates for the average brightness temperature $(T_v + T_h)/2$ are included because it is insensitive to the Faraday rotation. The third row provides the sensitivity of the brightness temperatures to SSS, indicating a varying degree of sensitivity versus polarization and water temperature. Rows 4 to 14 provide the residual brightness temperature errors after data corrections or under an assumed threshold for data flag. The net effect of geophysical errors is described in row 15 under the assumption that all the geophysical error sources are uncorrelated. The square root of the sum of squares (RSS) of every quantity is about 0.2 K and slightly smaller for the mid-range of water temperature. One of the dominant error sources is the surface roughness. It is assumed that coincidental radar measurements are available to reduce the errors to 0.1 K for T_v and T_h . As a reference, 0.1 K corresponds to a wind speed uncertainty of $0.5 \text{ m}\cdot\text{s}^{-1}$ for vertical polarization and $0.25 \text{ m}\cdot\text{s}^{-1}$ for horizontal polarization. The surface roughness error for $T_v - 0.6T_h$ does not assume a radar channel for correction and is assumed to be 0.1 K, which is probably the accuracy achievable by the simple linear correction model.

The sensor errors include the calibration errors and the radiometer noise-equivalent-delta-T (NEDT). The instrument calibration stability does not include the bias of the instrument calibration errors, and only accounts for the temporal variability of the instrument calibration. It is assumed that the instrument calibration bias is a constant and hence can be removed by a comparative analysis of in-situ measurements. The dominant errors sources are the antenna pointing angle, antenna emissivities, and the stability of calibration device, such as the noise source, for the electronics. A breakdown of the 0.2 K calibration stability is suggested in [11]. The radiometer NEDT is assumed to be 0.1 K for each polarization channel, which is achievable for the mission concept described in [11].

The total brightness temperature error is estimated to be about 0.3 K, which is depicted in the third row from the bottom of the table. The corresponding salinity error is shown

in the second row from the bottom. The vertical polarization outperforms the other polarization combinations because of its superior sensitivity to salinity, while the polarization difference $T_v - 0.6T_h$ yields the worst accuracy because of the least sensitivity to SSS. The average brightness temperature $(T_v + T_h)/2$ has the advantage of a negligible Faraday rotation error, but its performance is slightly worse than the vertical polarization because of a slight degradation of SSS sensitivity. The accuracy indicated here is for one satellite observation, and approaches 0.8 psu (vertical polarization) for cold waters and improves with increasing water temperatures with about 0.4 psu for warm waters.

To achieve a better accuracy, multiple independent observations are needed. The independent measurements can possibly result from temporal or spatial averaging. The temporal averaging involves the average of data from multiple satellite passes over a given surface grid cell. The revisit time is a few hours for high latitudes and 1 to 3 days for equatorial regions; therefore it is reasonable to assume that the data from different satellite passes are uncorrelated. In contrast, the spatial averaging over the measurements from adjacent antenna footprints may not reduce the error because most of the geophysical error sources discussed in Section 2 and instrument calibration uncertainty are likely to have a spatial correlation. For the conical scanner described in [11], a correlation time of a few minutes for the instrument calibration error will make the measurements across the entire swath and along the track of about 1000 km correlated. The only error source that definitely can be improved by spatial averaging is the sensor NEDT, which is random.

To be conservative, we assume only the measurements from different satellite passes as independent estimates. Under this assumption, the number of satellite passes required to reduce the error to 0.1 psu, indicated in the last row of Table 3, is about 60 for cold waters with vertical polarization and 14 for equatorial regions. It is indicated in Fig. 10(b) that one week sampling with a polar-orbiting instrument with 900 km swath results in about 6 passes in the equatorial areas and about 14 passes at high latitudes. This suggests that a weekly average accuracy of 0.2 psu is achievable with the vertical polarization data. An average of

the SSS estimates from both polarizations should yield better accuracy. An extrapolation of the above discussion to monthly average suggests that the salinity accuracy of 0.1 psu can be obtained for global monthly averaged gridded data set under the assumptions stated above.

4 Summary

A detailed analysis of various geophysical error sources that influence the microwave remote sensing of ocean surface salinity has been performed. Many of them are shown to have an influence of a few Kelvin, which are not negligible compared with the sensitivity of L-band sea surface brightness temperatures to salinity. An accurate knowledge of these parameters is necessary to enable a correction of the microwave measurements to accurately measure SSS.

A set of assumptions, which can be translated to the requirements on retrieval algorithms and instrument characteristics, have been explored to estimate the accuracy of global gridded salinity products. It is suggested that an accuracy of 0.1 psu is achievable for a monthly average gridded data set for a polar-orbiting satellite with a swath width of 900 km. Satellite instrument configurations with a smaller swath, but potentially less susceptible to various geophysical sources and easier for calibration, should be studied to find out whether a similar accuracy can be achieved.

A key factor to enable the accuracy of satellite measurements is the stability of the instrument or calibration device. The instrument has to be calibrated to an accuracy of better than 0.2 K in terms of temporal variability. This level of precision is believed to be achievable, but does represent an implementation challenge. Extreme care has to be taken for the sensor design and development.

ACKNOWLEDGMENT

The research described in this paper was carried out by the Jet Propulsion Laboratory, California Institute of Technology, under a contract with the National Aeronautics and Space Administration.

References

- [1] Lagerloef, Gary S. E., Preliminary Assessment of the Scientific and Technical Merits for Salinity Remote Sensing from Satellite, Report of the First Salinity Sea Ice Working Group Workshop, La Jolla, CA, 7-8 February 1998.
- [2] Swift, C. T. and R. E. McIntosh, "Considerations for Microwave Remote Sensing of Ocean Surface Salinity," *IEEE Trans. Geosci. Remote Sensing*, Vol. 21, No. 4, 480-491, 1983.
- [3] Blume, Hans-Juergen C., B. M. Kendall, and J. C. Fedors, "Measurement of Ocean Surface Temperature and Salinity via Microwave Radiometry," *Bound. Layer Meteor.*, 13, 295-308, 1978.
- [4] Lagerloef, G., C. T. Swift, and D. LeVine, "Sea Surface Salinity: The next remote sensing challenge," *Oceanography*, 8, 44-50, 1995.
- [5] Miller, J. L., M. A. Goodberlet, and J. B. Zaitzev, Airborne salinity mapper makes debut in coastal zone, EOS, Trans. AGU, 79, 173 and 176-177, 1998.
- [6] Le Vine, D. M., M. Kao, R. W. Garvine, and T. Sanders, "Remote sensing of ocean salinity: Results from the Delaware coastal current experiment," *J. Atmos. Oceanic Tech.*, Vol. 15, 1478-1484, 1998.
- [7] J. P. Hollinger, "Passive microwave measurements of sea surface roughness," *IEEE Trans. Geosci. Electronics*, Vol. GE-9, No. 3, 165-169, July 1971.
- [8] Klein, L. A., and C. T. Swift, "An improved model for the dielectric constant of sea water at microwave frequencies," *IEEE Trans. Ant. Prop.*, AP-25, 104-111, 1977.
- [9] Ellison, W., A. Balana, G. Delbos, K. Lamkaouchi, L. Eymard, C. Guillou, and C. Prigent, "New permittivity measurements of seawater," *Radio Science*, Vol. 33, No. 3, 639-648, 1998.
- [10] Guillou, C., W. Ellison, L. Eymard, K. Lamkaouchi, C. Prigent, G. Delbos, and A. Balana, "New permittivity measurements of seawater," *Radio Science*, Vol. 33, No. 3, 649-667, 1998.
- [11] Njoku, E. G., W. J. Wilson, S. H. Yueh, and Y. Rahmat-Samii, "A Large-Antenna Microwave Radiometer-Scatterometer Concept for Ocean Salinity and Soil Moisture Sensing," *IEEE Trans. Geosci. Remote Sensing*, in press.
- [12] Kraus, J. D., Radio Astronomy, 2nd. ed., 1986, Cygnus-Quasar Books, Powell, Ohio.
- [13] Martin-Neira, M., and J. M. Goutoule, "MIRAS-A two dimensional aperture/synthesis radiometers for soil moisture and ocean salinity observations," *ESA Bull.-European Space Agency*, 92, 95-104, 1997.
- [14] Swift, Calvin T., "Microwave radiometer measurements of the Cape Cod Canal," *Radio Science*, Vol. 9, No. 7, 641-653, 1974.
- [15] Webster, W. J., and T. T. Wilheit, Spectral Characteristics of the Microwave Emission From a Wind-Driven Foam-Covered Sea, *J. Geophys. Res.*, Vol. 81, No. 18, 3095-3099, June 1976.

- [16] Blume, Hans-Juergen C., A. W. Love, M. J. Van Melle and W. W. Ho, Radiometric Observations of Sea Temperatures at 2.65 GHz over the Chesapeake Bay, *IEEE Trans. Ant. Prop.*, Vol. AP-25, No. 1, 121-128, Jan 1977.
- [17] Liebe, H. J., An updated model for millimeter wave propagation in moist air, *Radio Science*, Vol. 20, No. 5, 1069-1089, 1985.
- [18] Sasaki, Yasunori, Ichio Asanuma, Kei Muneyama, Gen'Ichi Naito, and Tsutomu Suzuki, The dependence of sea-surface microwave emission on wind speed, frequency, incidence angle, and polarization over the frequency range from 1 to 40 GHz, *IEEE Trans. Geosci. and Remote Sensing*, Vol. GE-25, No. 2, 138-146, March, 1987.
- [19] M. A. Donelan and W. J. Pierson, "Radar scattering and equilibrium ranges in wind-generated waves with applications to scatterometry," *J. Geophys. Res.*, Vol. 92, No. c5, 4971-5029, May 15, 1987.
- [20] C. Rufenach, "A new relationship between radar cross-section and ocean surface wind speed during ERS-1 scatterometer and buoy measurements," *Int. J. Remote Sensing*, Vol. 16, No. 18, 3629-3647, 1995.
- [21] Tsang, L., J. A. kong, and R. T. Shin, *Theory of Microwave Remote Sensing*, Wiley Interscience, new York, 1985.
- [22] Trokhimovski, Yuri G., G. A. Bolotnikova, Valentin S. Etkin, Svetlana I. Grechko, and A. V. Kuzmin, The Dependence of S-band Sea Surface Brightness Temperatures on Wind Vector at Normal Incidence, *IEEE Trans. Geosci. Remote Sens.*, Vol. 33, No. 4, 1085-1088, July 1995.
- [23] Yueh, S. H., "Estimates Of Faraday Rotation With Passive Microwave Polarimetry For Microwave Remote Sensing Of Earth Surfaces," *IEEE Trans. Geosci. Remote Sensing*, in press.
- [24] Wilson, B. D., A. J. Mannucci, and C. D. Edwards, "Subdaily northern hemisphere ionospheric maps using an extensive network of GPS receivers," *Radio Science*, Vol. 30, No. 3, 639-648, May-June, 1995.

List of Tables

1	The coefficients of the empirical model for the atmospheric propagation loss and radiation from gases and water vapor. $\alpha = a_0 + a_1T_s + a_2T_s^2 + bV$ where T_s is the surface air temperature in °C and V is the columnar water vapor height in cm.	27
2	Sensitivity of sea surface brightness temperatures to surface wind speed W ($\text{m}\cdot\text{s}^{-1}$).	28
3	Summary of geophysical and instrument error sources as well as estimates of salinity retrieval error per satellite pass for a spaceborne L-band microwave radiometer operating at 40° incidence.	29

α	a_0	a_1	a_2	b
β (dB)	0.0104	-0.000027	0.0000	0.0000
T_u, T_d (K)	2.588	0.0008	-0.00013	0.0002

Table 1: The coefficients of the empirical model for the atmospheric propagation loss and radiation from gases and water vapor. $\alpha = a_0 + a_1 T_a + a_2 T_a^2 + bV$ where T_a is the surface air temperature in °C and V is the columnar water vapor height in cm.

Frequency (GHz)	Polarization	Incidence Angle (Deg)	ΔT_b (K)	Reference
1.4	V	20	0.15 W	Hollinger [7]
1.4	V	40	0.13 W	Hollinger [7]
1.4	V	55	0.02 W	Hollinger [7]
1.4	H	20	0.2 W	Hollinger [7]
1.4	H	40	0.2 W	Hollinger [7]
1.4	H	55	0.35 W	Hollinger [7]
1.4	H	23	0.25 W	Swift [14], Sasaki et al. [18]
1.4	H	40	0.4 W	Swift [14], Sasaki et al. [18]
1.4	H	53	0.45 W	Swift [14], Sasaki et al. [18]
1.4	Linear	0	0.16 W	Webster et al. [15]
2.65	Linear	0	$0.27 W^{0.53}$	Blume et al. [16]
3.76	Linear	0	$0.67 W^{0.84}$	Trokhimovski et al. [22]
3.76	Linear	0	0.45 W	Trokhimovski et al. [22]
1.4	V	40	0.23 W	JPL Gulf-Stream Flights in July 1999
1.4	H	40	0.40 W	JPL Gulf-Stream Flights in July 1999

Table 2: Sensitivity of sea surface brightness temperatures to surface wind speed W ($\text{m}\cdot\text{s}^{-1}$).

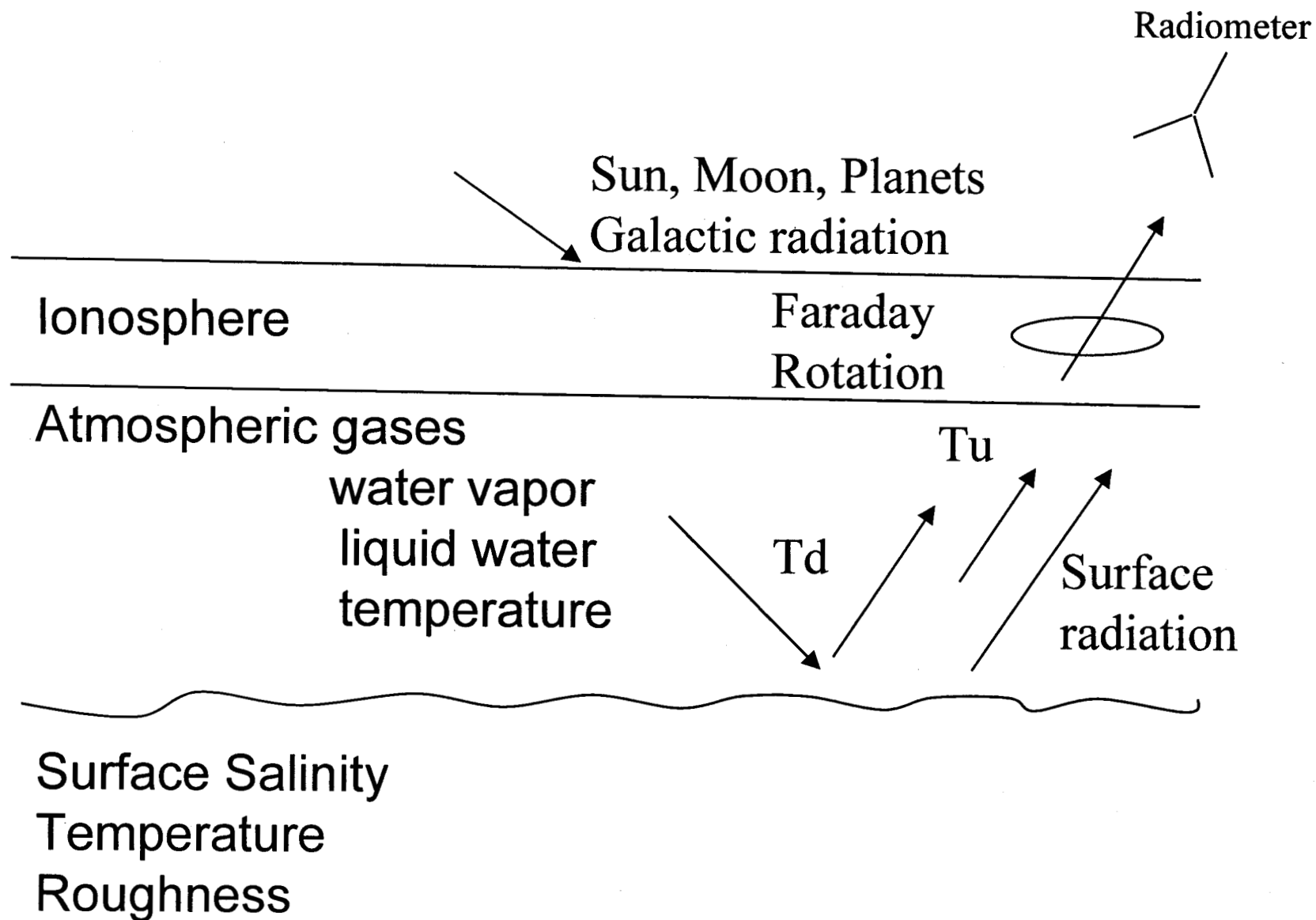
Parameter	Knowledge	0-10 deg C				10-20 deg C				25-35 deg C			
Polarization		V	H	(V+H)/2	V-0.6H	V	H	(V+H)/2	V-0.6H	V	H	(V+H)/2	V-0.6H
dTb/dSSS (K/psu)		0.40	0.30	0.35	0.22	0.55	0.40	0.48	0.31	0.80	0.60	0.70	0.44
SST	0.5 deg C	0.08	0.04	0.06	0.06	0.01	-0.02	0.00	0.02	-0.08	-0.07	-0.07	-0.04
Dry Air	10 deg C Temperature	0.14	0.16	0.15	0.04	0.11	0.13	0.12	0.03	0.10	0.10	0.10	0.04
Cloud	0.15 mm	0.04	0.04	0.04	0.02	0.04	0.04	0.04	0.02	0.04	0.04	0.04	0.02
Water Vapor	3 cm	0.01	0.01	0.01	0.00	0.01	0.01	0.01	0.00	0.01	0.01	0.01	0.00
Faraday Rotation	0.2 deg	0.06	0.06	0.01	0.09	0.06	0.06	0.01	0.09	0.06	0.09	0.01	0.09
Sun	Correction and Threshold	0.05	0.05	0.05	0.02	0.05	0.05	0.05	0.02	0.05	0.05	0.05	0.02
Moon	Threshold of Data Flag	0.01	0.01	0.01	0.01	0.01	0.01	0.01	0.01	0.01	0.01	0.01	0.01
Planets	Threshold of Data Flag	0.01	0.01	0.01	0.01	0.01	0.01	0.01	0.01	0.01	0.01	0.01	0.01
Galactic	Threshold of Data Flag	0.01	0.01	0.01	0.01	0.01	0.01	0.01	0.01	0.01	0.01	0.01	0.01
Hydrogen Line	1%	0.05	0.05	0.05	0.02	0.05	0.05	0.05	0.02	0.05	0.05	0.05	0.02
Surface Roughness	Radar Corr. or Modeling Unc.	0.10	0.10	0.10	0.10	0.10	0.10	0.10	0.10	0.10	0.10	0.10	0.10
RSS of Geophysical Error (K)		0.22	0.22	0.21	0.16	0.18	0.19	0.18	0.14	0.19	0.20	0.18	0.15
Sensor Calibration Stability (K)		0.20	0.20	0.20	0.20	0.20	0.20	0.20	0.20	0.20	0.20	0.20	0.20
Sensor Delta T (K)		0.10	0.10	0.07	0.12	0.10	0.10	0.07	0.12	0.10	0.10	0.07	0.12
RSS of Total Tb Error (K)		0.31	0.31	0.30	0.28	0.29	0.30	0.28	0.27	0.29	0.30	0.28	0.28
Salinity Accuracy (psu) Per Obs.		0.78	1.04	0.85	1.28	0.52	0.74	0.58	0.89	0.37	0.50	0.40	0.63
Number of Samples for 0.1 psu		60	109	72	163	27	55	33	78	14	25	16	40

Table 3

List of Figures

1	Geophysical sources that will influence the microwave radiation from sea surfaces.	32
2	The sensitivity of sea surface brightness temperatures to water salinity at 40° incidence, predicted by the Ellison model [9]. The two upper panels plot T_v and T_h versus the salinity at six water temperatures. The two lower panels plot the derivatives to indicate the sensitivity to SSS.	33
3	The sensitivity of sea surface brightness temperatures to water salinity versus incidence angle, predicted by the Ellison model [9] for a salinity of 35 psu. The upper panel is for T_v , the middle panel for T_h , and the lower panel for $(T_v + T_h)/2$	34
4	The sensitivity of sea surface brightness temperatures to water temperature versus incidence angle, predicted by the Ellison model [9] for a salinity of 35 psu. The upper panel is for T_v , the middle panel for T_h , and the lower panel for $(T_v + T_h)/2$	35
5	Microwave radiation and attenuation at 1.4 GHz by atmospheric dry air and water vapor estimated from the NCEP/NCAR reanalyses. β is the transmissivity. T_u and T_d are the upwelling and downwelling emission temperatures, respectively.	36
6	Microwave radiation and attenuation from non-raining clouds at 1.4 GHz along the nadir path.	37

7	L-band microwave radiometer and radar observations of sea surfaces at 40° incidence acquired on July 17, 1999, near the Gulf Stream off Norfolk, Virginia. The upper panel plots the vertically and horizontally polarized brightness temperatures. T_v and T_h are the sensor data. The curves labeled by "Corr." are the data subtracted by $A\sigma_{hh}$ with $A = 400$ for T_h and 200 for T_v . The second panel from the top plots the normalized radar cross section (NRCS) for vertically polarized transmit and receive (VV) and horizontally polarized transmit and receive (HH). The two lower panels plot the SSS retrieved from the data illustrated in the upper panel.	38
8	Mechanisms of solar radiation leakage into the spaceborne microwave system.	39
9	Estimates of solar radiation and reflection at 1.4 GHz.	40
10	Sampling frequency of earth surfaces by a microwave imaging system for one week under the assumption of 900 km swath width for a sun-synchronous polar orbit at 600 km altitude. (a) The spatial sampling map, and (b) the sampling statistics for 1-degree latitude by 1-degree longitude bins for every 10-degree latitude.	41



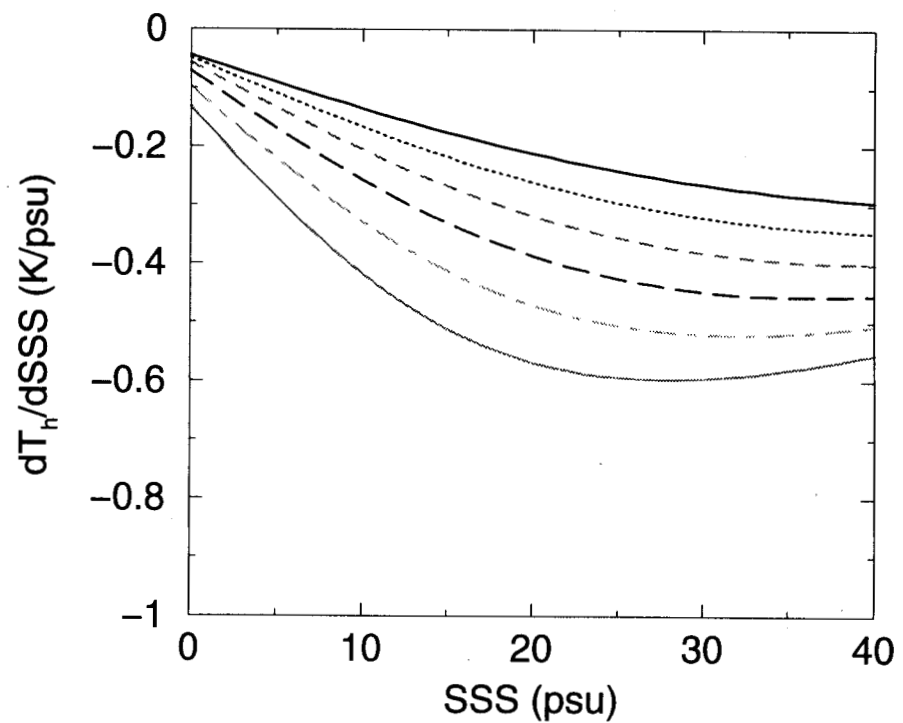
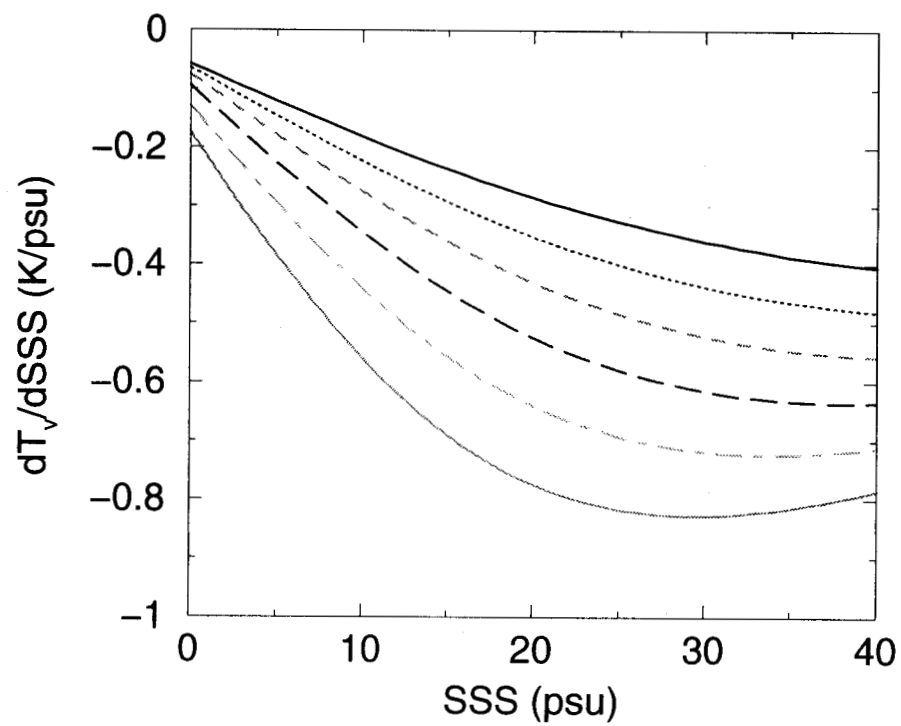
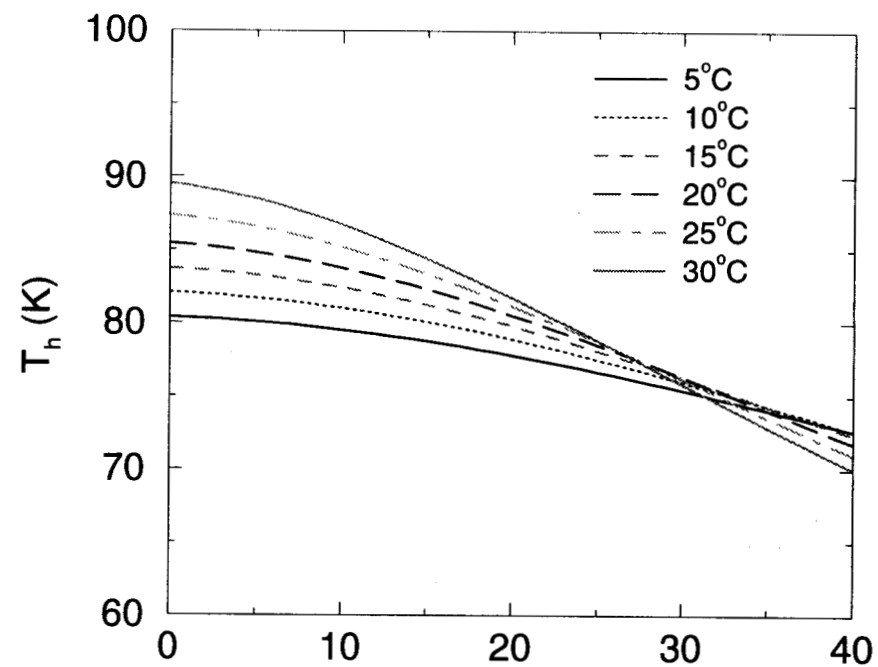
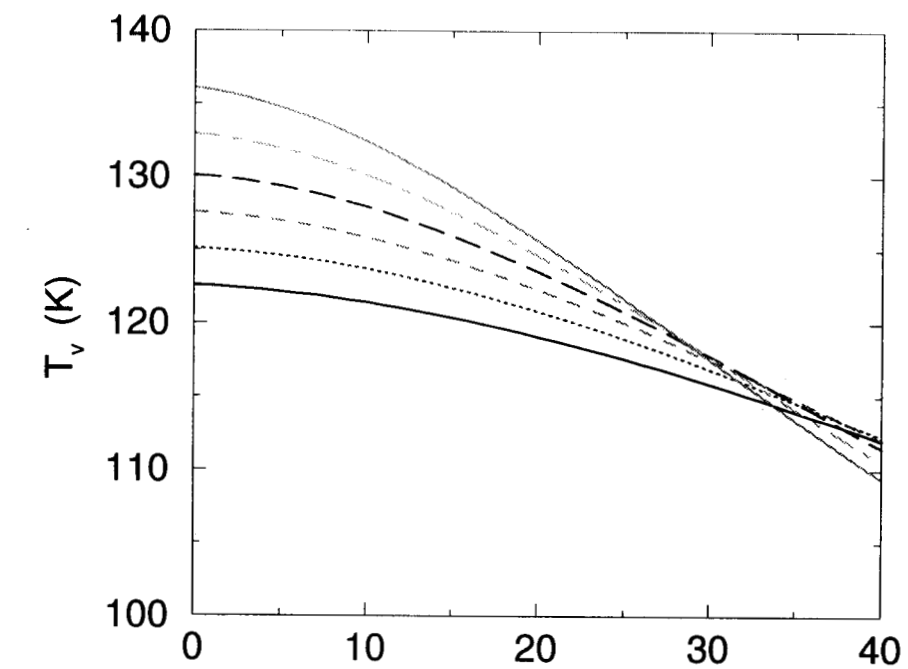


Fig. 2

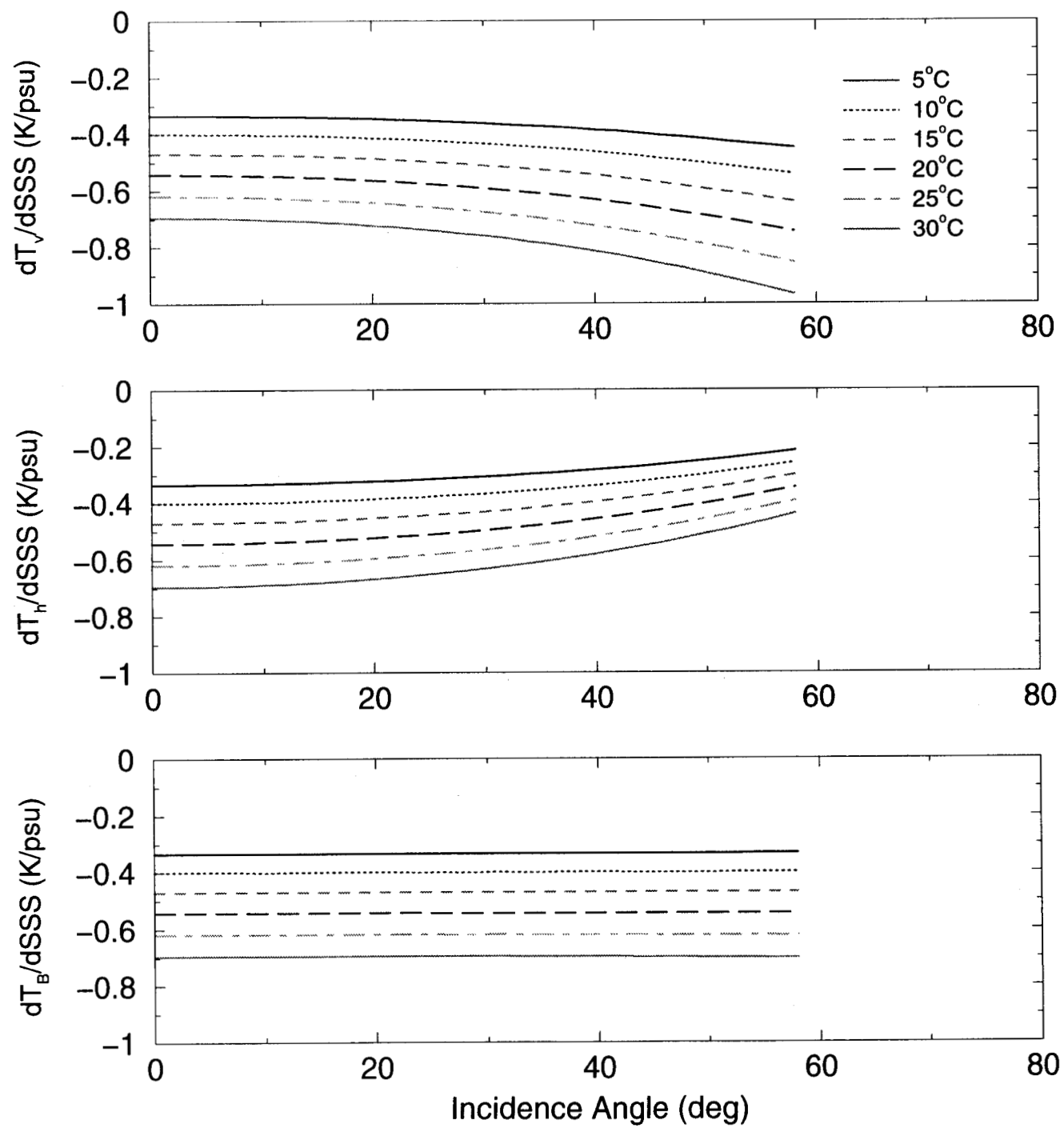


Fig. 3

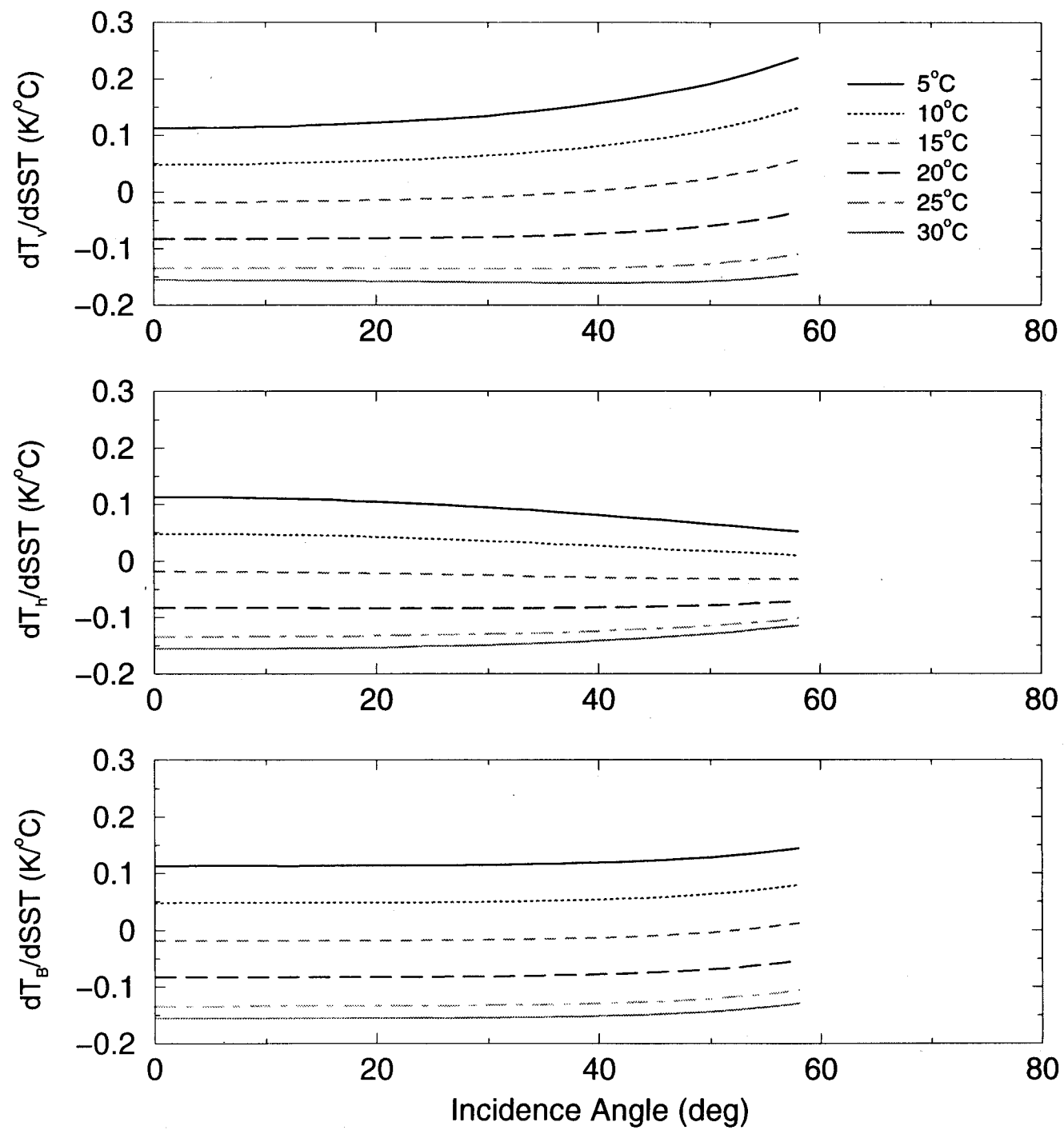


Fig. 4

ATMOSPHERIC RADIATION AND ATTENUATION (1400 MHz) – 1995

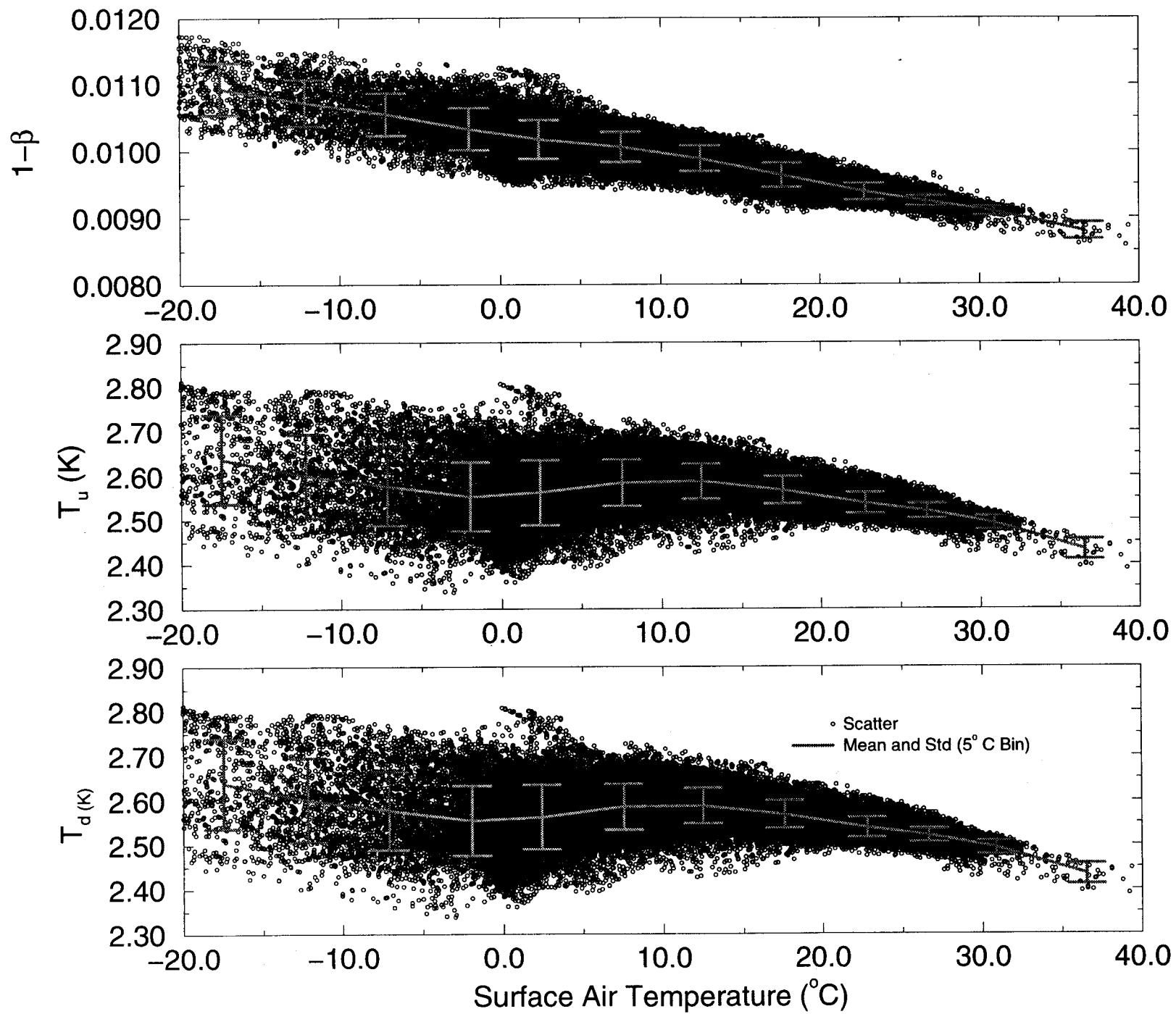


Fig. 5

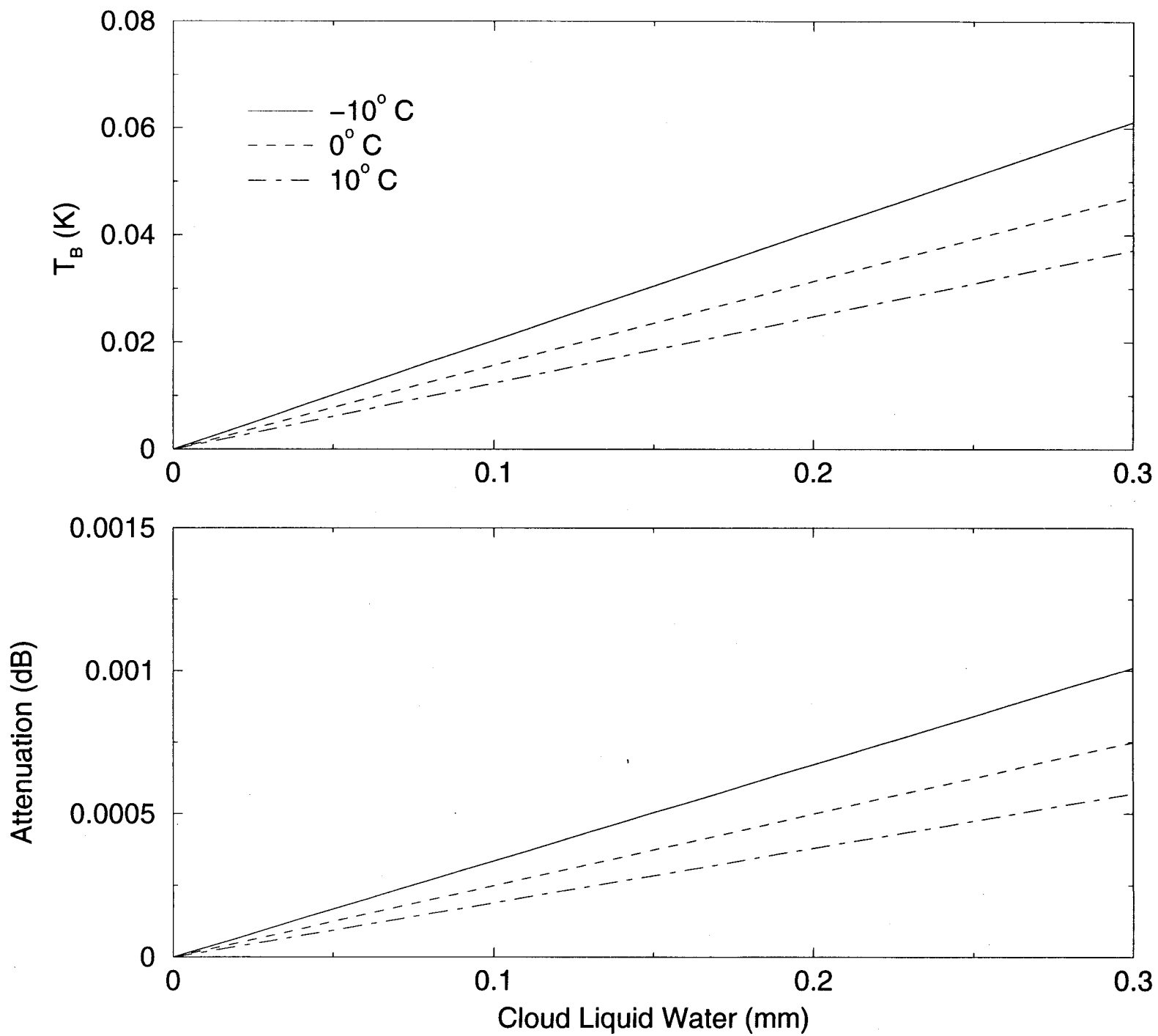


Fig. 6

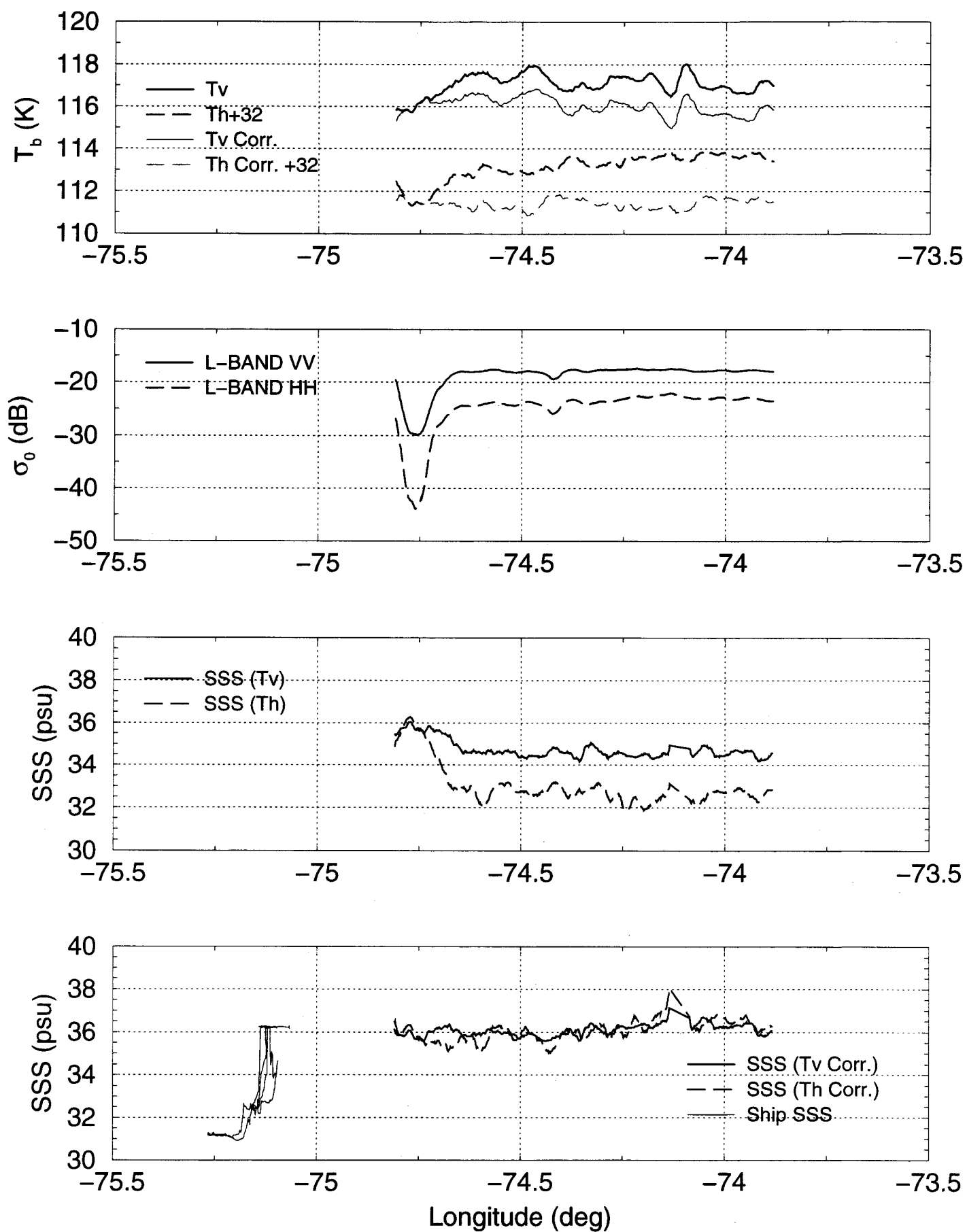


Fig. 7

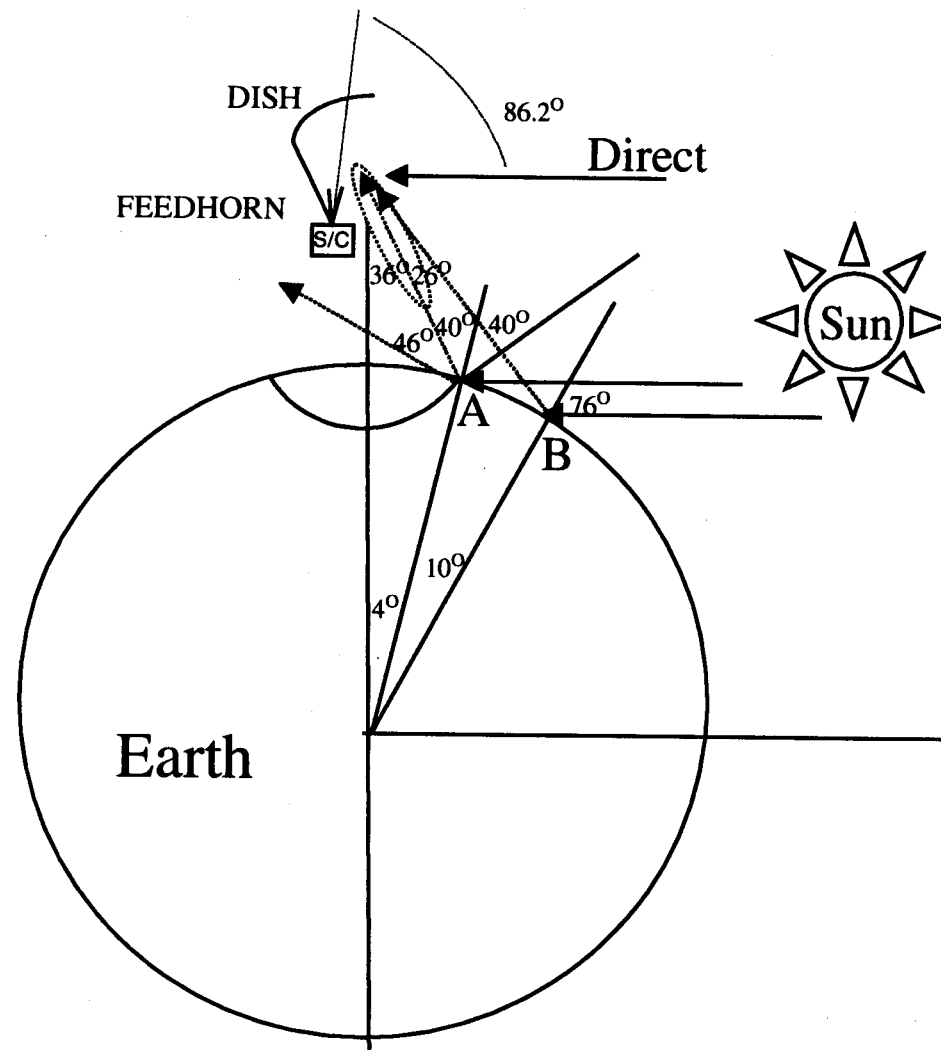


Fig. 8

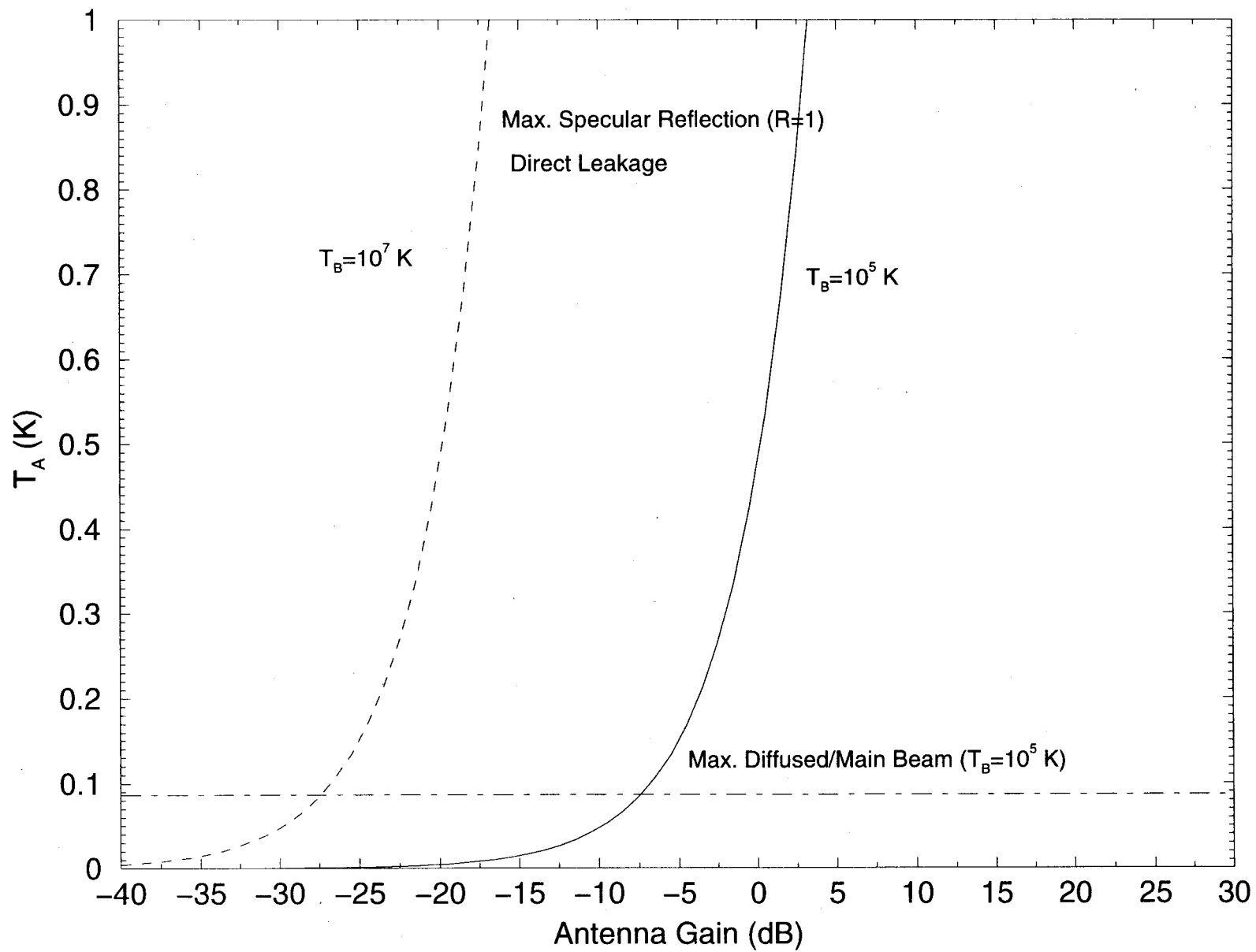


Fig. 9

Satellite Sampling Map With A Conical-Scanner for 1 Week

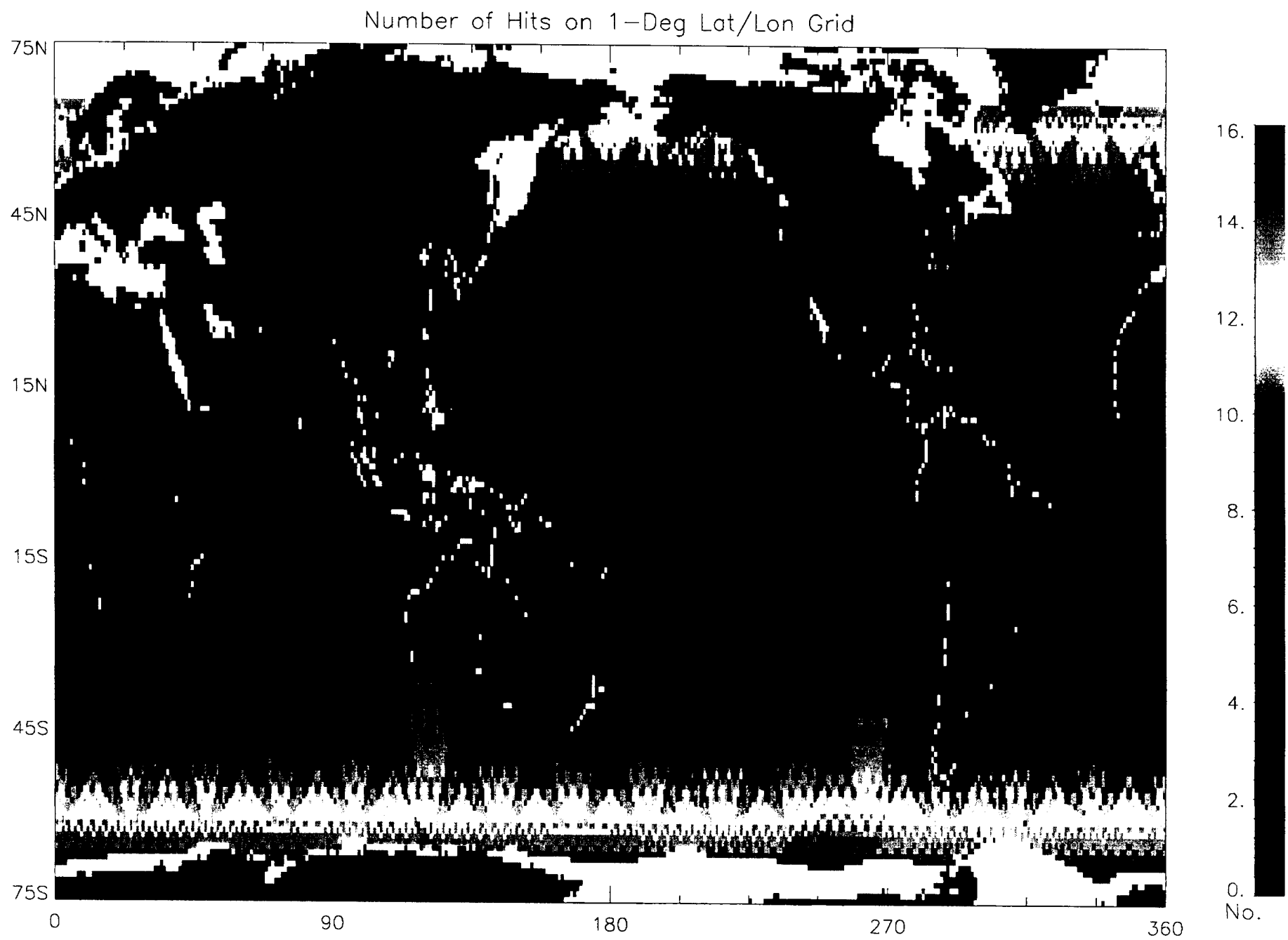


Fig. 10(a)

Satellite Coverage with A Conical Scanner for 7 Days

